radius apertures following the standard prescription[28]. Additional corrections were made as follows: (1) +0.05 mag to correct for the so-called 'long exposure' effect[29]; (2) −0.04 mag, which is the appropriate colour term to convert to standard Cousin's I magnitudes for red stars with $V - I \approx 1.5$ (ref. 28); and (3) −0.04 mag to allow for the expected foreground extinction[30]. We estimate that the combined uncertainty from the zero-point calibration and the various correction terms amounts to 0.06 mag. Clearly extended sources were removed from the catalogue by restricting our analysis to sources with a DAOPHOT sharpness parameter $-0.6 < s < 0.4$. A similar procedure was also followed for the HDF control field. Finally, we created 12 test data sets in which 265 simulated stars were added to the real data frames. The input magnitudes of the simulated stars covered the range from 23.5 to nearly 30. We then processed these frames in the same way as the original data, and produced a matrix relating the recovered magnitudes and detection efficiency to the input magnitudes of the simulated stars. From these simulations we estimate that the catalogue is ~80% complete at $I = 27.9$, and use this as the limiting magnitude in our analysis.

Received 27 June; accepted 25 November 1997.

1. Zwicky, F. The Coma cluster of galaxies. *Publ. Astron. Soc. Pacif.* **63,** 61–71 (1951).
2. Merritt, D. Relaxation and tidal stripping in rich clusters of galaxies. ii—Evolution of the luminosity distribution. *Astrophys. J.* **276,** 26–37 (1984).
3. Moore, B., Katz, N., Lake, G., Dressler, A. & Oemler, A. J. Galaxy harassment and the evolution of clusters of galaxies. *Nature* **379,** 613–616 (1996).
4. de Vaucouleurs, G. The apparent density of matter in groups and clusters of galaxies. *Astrophys. J.* **131,** 585–597 (1960).
5. Gunn, J. E. Visual background radiation in the Coma cluster of galaxies. *Bull. Am. Astron. Soc.* **1,** 191 (1969).
6. Thuan, T. X. & Kormendy, J. Photographic measurements of diffuse light in the Coma cluster. *Publ. Astron. Soc. Pacif.* **89,** 466–473 (1977).
7. Uson, J. *et al.* Diffuse light in dense clusters of galaxies. i—R-band observations of Abell 2029. *Astrophys. J.* **369,** 46–53 (1991).
8. Vilchez-Gomez, R. *et al.* Detection of intracluster light in the rich clusters of galaxies Abell 2390 and cl1613+31. *Astron. Astrophys.* **283,** 37–50 (1994).
9. Scheick, X. & Kuhn, J. R. Diffuse light in A2670: Smoothly distributed? *Astrophys. J.* **423,** 566–580 (1994).
10. Arnaboldi, M. *et al.* The kinematics of the planetary nebulae in the outer regions of NGC 4406. *Astrophys. J.* **472,** 145–152 (1996).
11. Theuns, T. & Warren, S. J. Intergalactic stars in the Fornax cluster. *Mon. Not. R. Astron. Soc.* **284,** L11–L15 (1996).
12. Miller, G. E. Effects of galaxy collisions on the structure and evolution of galaxy. *Astrophys. J.* **268,** 495–512 (1983).
13. Moore, B., Katz, N. & Lake, G. On the destruction and overmerging of dark halos in dissipationless n-body simulations. *Astrophys. J.* **457,** 455–459 (1996).
14. Peebles, P. J. E. Statistical analysis of catalogs of extragalactic objects vi. The galaxy distribution in the jagellonian field. *Astrophys. J.* **196,** 647–652 (1975).
15. Brainerd, T. G., Smail, I. & Mould, J. The evolution in clustering of galaxies to R = 26. *Mon. Not. R. Astron. Soc.* **275,** 781–789 (1995).
16. Bertelli, G., Bressan, A., Chiosi, C., Fagotto, G. & Nasi, E. Theoretical isochrones from models with new radiative opacities. *Astron. Astrophys. Suppl. Ser.* **106,** 275–302 (1994).
17. Sakai, S. *et al.* Detection of the tip of the red giant branch in NGC 3379 (M105) in the Leo I group using the Hubble Space Telescope. *Astrophys. J.* **478,** 49–57 (1997).
18. Capaccioli, M., Held, E. V., Lorenz, H. & Vietri, M. Photographic and CCD surface photometry of the standard elliptical galaxy NGC3379. *Astron. J.* **99,** 1813–1822 (1990).
19. Tanvir, N. R., Shanks, T., Ferguson, H. C. & Robinson, D. R. T. Determination of the Hubble constant from observations of cepheid variables in the galaxy M96. *Nature* **377,** 27–31 (1995).
20. Tully, R. B. & Shaya, E. J. Infall of galaxies into the Virgo cluster and some cosmological constraints. *Astrophys. J.* **281,** 31–55 (1984).
21. Binggeli, B., Sandage, A. & Tammann, G. A. Studies of the Virgo cluster. ii—a catalog of 2096 galaxies in the Virgo cluster area. *Astron. J.* **90,** 1681–1771 (1985).
22. Caon, N., Capaccioli, M. & Rampazzo, R. Photographic and CCD surface photometry of 33 early-type galaxies in the Virgo cluster. *Astron. Astrophys. Suppl. Ser.* **86,** 429–471 (1990).
23. Freedman, W. L. *et al.* Distance to the Virgo cluster galaxy M100 from Hubble Space Telescope observations of cepheids. *Nature* **371,** 757–762 (1994).
24. Sandage, A. & Tammann, G. An alternative calculation of the distance to M87 using the Whitmore et al. luminosity function for its globular clusters: H0 therefrom. *Astrophys. J.* **464,** L51–L54 (1996).
25. Nulsen, P. E. J. & Böhringer, H. A Rosat determination of the mass of the central Virgo cluster. *Mon. Not. R. Astron. Soc.* **274,** 1093–1106 (1995).
26. Lee, M. G., Freedman, W. L. & Madore, B. F. Astrophys. J. **417,** 553–559 (1993).
27. Soria, R. *et al.* Detection of the tip of the red giant branch in NGC5128. *Astrophys. J.* **465,** 79–90 (1996).
28. Holtzman, J. A. *et al.* The photometric performance and calibration of WFPC2. *Publ. Astron. Soc. Pacif.* **107,** 1065–1093 (1995).
29. Hill, R. J. *et al.* The extragalaxtic distance scale key project. V. Photometry of the brightest stars in M100 and the calibration of WFPC2. *Astrophys. J.* (in the press).
30. Burstein, D. & Heiles, C. Reddening estimates for galaxies in the second reference catalog and the Uppsala general catalog. *Astrophys. J. Suppl. Ser.* **54,** 33–79 (1984).
31. Williams, R. E. *et al.* The Hubble deep field: Observations, data reduction, and galaxy photometry. *Astron. J.* **112,** 1335–1389 (1996).
32. Salpeter, E. E. The luminosity function and stellar evolution. *Astrophys. J.* **121,** 161–167 (1955).
33. Stetson, P. B. DAOPHOT-A computer program for crowded-field stellar photometry. *Publ. Astron. Soc. Pacif.* **99,** 191–222 (1987).

Acknowledgements. We thank S. Sakai, R. Soria and C. Grillmair for providing stellar photometry from nearby galaxies for comparison to the Virgo Cluster data; M. Dickinson for the use of the 3C210 comparison field; to A. Fruchter and R. Hook for use of the 'drizzle' code; V. Rubin, F. Schweizer and A. Saha for discussions; and the Department of Terrestrial Magnetism for hospitality (T.v.H.). T.v.H. was partially supported by the Edgar P. and Nona B. McKinney Charitable Trust. This work was also supported by NASA through a General Observer research grant awarded by Space Telescope Science Institute, which is operated by the Association of Universities for Research in Astronomy.

Correspondence and requests for materials should be addressed to H.C.F. (e-mail: ferguson@stsci.edu).

Phase matching using an isotropic nonlinear optical material

A. Fiore, V. Berger, E. Rosencher, P. Bravetti & J. Nagle

Thomson CSF Laboratoire Central de Recherches, Domaine de Corbeville, 91400 Orsay, France

Frequency conversion in nonlinear optical crystals[1,2] is an effective means of generating coherent light at frequencies where lasers perform poorly or are unavailable. For efficient conversion, it is necessary to compensate for optical dispersion, which results in different phase velocities for light of different frequencies. In anisotropic birefringent crystals such as $LiNbO_3$ or KH_2PO_4 ('KDP'), phase matching can be achieved between electromagnetic waves having different polarizations. But this is not possible for optically isotropic materials, and as a result, cubic materials such as GaAs (which otherwise have attractive nonlinear optical properties) have been little exploited for frequency conversion applications. Quasi-phase-matching schemes[1,3], which have achieved considerable success in $LiNbO_3$ (ref. 4), provide a route to circumventing this problem[5,6], but the difficulty of producing the required pattern of nonlinear properties in isotropic materials, particularly semiconductors, has limited the practical utility of such approaches. Here we demonstrate a different route to phase matching—based on a concept proposed by Van der Ziel 22 years ago[7]—which exploits the artificial birefringence of multilayer composites of GaAs and oxidised AlAs. As GaAs is the material of choice for semiconductor lasers, such optical sources could be integrated in the core of frequency converters based on these composite structures.

Optical frequency conversion[1,2] by second-order nonlinear interaction is a way to obtain coherent light in various spectral regions. The frequency doubling process is used, for instance, to obtain green light from the very efficient near-infrared YAG laser, whereas difference frequency generation (DFG) is the basic process for high-power mid-infrared sources such as optical parameter oscillators. The best known nonlinear materials used for frequency conversion are KDP or $LiNbO_3$ (ref. 2), but several other crystals can be used; for example, KTP ($KTiOPO_4$), $AgGaSe_2$, GaAs, and synthetic materials as organic molecules or semiconductor quantum wells[8]. Among the different characteristics of nonlinear crystals, two are of paramount importance. (1) The nonlinear coefficient $\chi^{(2)}$, which is a measure of the strength of the nonlinear interaction, and is related to the degree of asymmetry of the electronic potential at the microscopic level. (2) The ability to match the phase velocities between the different frequencies[1]: owing to the optical dispersion of the nonlinear materials, the different waves do not travel at the same velocity in the material. After a distance called the 'coherence length', the nonlinear polarization and the generated wave acquire a phase lag of π, which produces a destructive interference. The effective conversion length is thus limited to the coherence length, which is often as small as a few micrometres. In reciprocal space, the phase-matching conditions expresses the photon momentum conservation.

To increase the coherence length, phase matching can be obtained in birefringent crystals as KDP or $LiNbO_3$; the polarizations of the different waves are carefully chosen in order to adjust their different phase velocities. GaAs is a very interesting material for nonlinear frequency conversion, because its huge nonlinear coefficient ($\chi^{(2)} \approx 240\,\mathrm{pm\,V^{-1}}$) gives about one order of magnitude greater efficiency that the commonly used materials. However, as it is an optically isotropic (cubic) semiconductor, it is non-birefringent and

phase matching is impossible. To use this highly nonlinear material in spite of the problem of phase matching, quasi-phase-matching[1,3] has been used. The sign of the nonlinear interaction is changed periodically by reversing the orientation of the material, in order to compensate for the periodic destructive interference due to phase mismatch. This technique has produced impressive results for $LiNbO_3$ (ref. 4), but although quasi-phase-matching has been shown in GaAs for both second-harmonic[5] and difference-frequency[6] generations, patterning the nonlinear susceptibilities is much more difficult in semiconductors. The technological steps necessary to obtain the material are difficult and the final materials suffer from detrimental losses.

Here we demonstrate perfect phase matching using an isotropic material as a microscopic nonlinear source. Phase matching is obtained by using a built-in artificial birefringence in a new composite multilayer material: the isotropy of bulk GaAs is broken by inserting thin oxidized AlAs ('Alox') layers in GaAs. The resulting composite material is not isotropic, and this is used to get birefringent phase matching, but the only nonlinear material present in the structure is the isotropic GaAs. The use of this so-called form birefringence[9,10] for nonlinear frequency conversion was proposed in 1975 by Van der Ziel[7]. Since then, however, the experimental realization of this proposal has not been achieved, because it has not been possible to find a well suited couple of materials having a high nonlinear coefficient and a high enough refractive index contrast for form birefringence phase matching.

A first, intuitive, way to understand the origin of form birefringence is to consider the macroscopic crystal formed by a GaAs/Alox multilayer system. GaAs is a cubic semiconductor of point group $\bar{4}3m$, and is therefore non-birefringent. The presence of thin Alox layers grown on a (100) substrate breaks the symmetry of three-fold rotation axes and the point group of the composite material is now $\bar{4}2m$, the same as KDP. This artificial material has the nonlinear properties of GaAs (in particular, the same tensorial character and roughly the same nonlinear coefficient, if we neglect the small reduction of the average nonlinear susceptibility due to the zero contribution of the thin Alox layers), but the linear optical symmetry of KDP. This is possible by taking advantage of the microscopic nature of the nonlinear polarization in GaAs and the macroscopic engineering of the refractive index on the scale of the extended electromagnetic wavelengths. We note that with (111) orientated GaAs, the introduction of Alox layers switches the point group from $\bar{4}3m$ to $3m$, which is that of another nonlinear material, $LiNbO_3$; the same birefringence properties are of course expected.

Van der Ziel[7] calculated form birefringence in the multilayer system directly from Maxwell's equations. Another physical explanation can be given using modal wavefunction considerations. We consider a periodic multilayer material, with light propagating in the plane of the layers. Following Joannopoulos[11], for a given wavevector the frequency of an allowed electromagnetic mode in a composite medium increases with the fraction of electric field in the low-index material. The difference between the transverse electric (TE) and transverse magnetic (TM) polarizations then arises from the continuity equations at the boundaries between the two materials, as illustrated in Fig. 1. In the TM polarization, the continuity of the electric displacement forces the electric field to have a large value in the low-index material; this mode therefore has a higher frequency ω for a given wavevector k. For a large wavelength compared to the unit cell, the light experiences an effective medium, that is, a homogeneous-like material, the inhomogeneities of the dielectric constant being averaged on the wavelength scale. This is why the dispersion relation $\omega(k)$ in Fig. 1 is linear at the origin. Form birefringence then appears as the difference between the slopes of the dispersion relations for TE and TM waves. In this long-wavelength

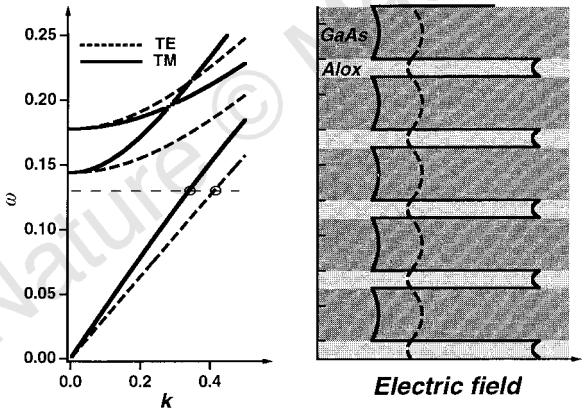

Figure 1 Dispersion relation for an in-plane propagation in a periodic composite material of period d. The material consists of 25% of Alox (refractive index $n \approx 1.6$; see text) and 75% of GaAs ($n \approx 3.5$), for TM modes (full line) and TE modes (dotted lines). The physical origin of form birefringence appears in the mode wavefunction, pictured on the left for a frequency $\omega = 0.13(2\pi/d)$ (corresponding to the open circles in the dispersion relation). These Bloch waves have been calculated using standard periodic multilayer theory[10]. The direction of propagation is perpendicular to the plane of the figure. Due to the continuity of the electric displacement ϵE normal to the layers, the TM mode (solid line in both panels) has a significant overlap with the low-ϵ layer (Alox, shown in light grey in the right panel), and a lower average dielectric constant. The continuous TE electric field (dotted line in both panels) has a higher value in GaAs (dark grey, right panel), and a higher average dielectric constant.

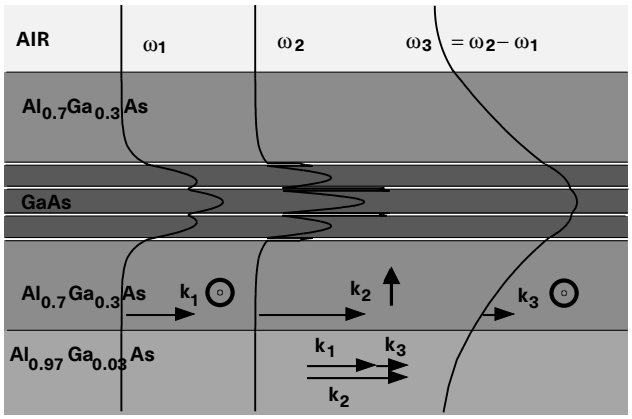

Figure 2 Difference frequency generation (DFG) process in the sample. Here ω_1 and ω_2 are the pump frequencies of wavelengths 1.32 μm and 1.058 μm, respectively, and ω_3 is the frequency difference of wavelength 5.3 μm. Three periods of the composite material GaAs (325 nm)/Alox (40 nm) constitute the core of the waveguide. The birefringence of the composite material was engineered to compensate for the dispersion arising from both the natural dispersion in bulk GaAs and the optical confinement dispersion in the waveguide. The sample was grown by molecular beam epitaxy on a GaAs (100) substrate and consists of: 2,800 nm $Al_{0.97}Ga_{0.03}As$; 1,500 nm $Al_{0.70}Ga_{0.30}As$ (waveguide cladding layers), three periods of birefringent composite material (40 nm Alox; 325 nm GaAs) × 3 and 40 nm Alox; 1,500 nm $Al_{0.70}Ga_{0.30}As$ and a final 30-nm GaAs cap layer. The oxidation process is described in detail in ref. 15. The three modes involved in the DFG process are pictured together with their polarization (↑ for TM, ⊙ for TE). The higher overlap of the TM mode with the low-refractive-index Alox layers is apparent, which is the origin of form birefringence. The arrows indicate the "phase matching" momentum conservation. $\mathbf{k}_1 + \mathbf{k}_3 = \mathbf{k}_2$, where $\mathbf{k}_i$ indicates the wavevector of the wavenumber i.

approximation, the two dielectric constants of the uniaxial composite material are given by:

$$\epsilon_{TE} = \alpha_1\epsilon_1 + \alpha_2\epsilon_2 \quad (1)$$

$$\frac{1}{\epsilon_{TM}} = \frac{\alpha_1}{\epsilon_1} + \frac{\alpha_2}{\epsilon_2} \quad (2)$$

where α_i and ϵ_i are the filling factors ($\alpha_1 + \alpha_2 = 1$) and the dielectric constant, respectively, of the two constitutive materials 1 and 2. These equations are analogous to electrical series and parallel capacitors. This is not surprising, because the charge equality $C_1V_1 = C_2V_2$ between series capacitors 1 and 2 is nothing but the static limit of the electric displacement continuity relation for TM waves $\epsilon_1E_1 = \epsilon_2E_2$, and the bias equality $V_1 = V_2$ for parallel capacitors 1 and 2 is equivalent to the electric-field continuity for TE waves $E_1 = E_2$. (Here C represents capacitance, and V voltage.)

It appears from equations (1) and (2) that form birefringence ($\sqrt{\epsilon_{TE}} - \sqrt{\epsilon_{TM}}$) increases with the refractive-index contrast between the two materials in the multilayer, as do photonic bandgap effects in photonic crystals[11]. Although form birefringence in a GaAs/AlGaAs multilayer structure has been proposed for phase matching[7], the refractive-index contrast between GaAs ($n \approx 3.5$) and AlAs ($n \approx 2.9$) is too low to provide the birefringe required to compensate for the dispersion. This is why we have used thin-film layers of Alox ($n \approx 1.6$) in GaAs to get sufficient form birefringence. Alox results from selective oxidation (at 400–500 °C in a water-vapour atmosphere) of AlAs layers embedded in GaAs. The technology of AlAs oxidation emerged[12] in the early 1990s; since then Alox has led to significant advances in the field of semiconductor lasers[13] and Bragg mirrors[14] thanks to its refractive index contrast with GaAs.

We have demonstrated phase matching of a DFG process in a waveguide containing four Alox layers. The structure which was used for the DFG is shown in detail in Fig. 2, together with the three modes involved in the nonlinear interaction.

We first characterized the form birefringence of the sample. The details of this experiment, using surface emitting second-harmonic generation, are given in ref. 15. A form birefringence $n_{TE} - n_{TM} = 0.154$ was measured. Even higher birefringences of the order of 0.2 have been obtained with different samples. This birefringence is sufficient to phase-match mid-infrared generation between 3 μm and 10 μm by DFG. We note that by increasing the width of Alox layers (as in the example of Fig. 1), much higher birefringences up to 0.65 could be achieved, but this is not necessary here.

For the DFG experiment, two continuous-wave pump lasers (a Nd:YAG with wavelength $\lambda = 1.32$ μm, and a tunable Titanium: Sapphire (Ti : Sa) were end-fire coupled in a 4-μm-wide, 1.2-mm-long channel waveguide. Using the $\chi^{(2)}_{xyz}$ element of GaAs, the DFG process was:

$$(1.058\ \mu m, TM) - (1.32\ \mu m, TE) \mapsto (5.3\ \mu m, TE) \quad (3)$$

as it appears in Fig. 2. The infrared signal is shown in Fig. 3 as a function of the Ti:Sa wavelength. This function has the well known $((\sin x)/x)^2$ shape, which is clear evidence of phase matching. All the polarization selection rules for equation (3) have been checked. These experiments show that perfect phase matching has been achieved with a cubic nonlinear material.

A mid-infrared output power of 80 nW was obtained for 0.4 mW and 11.6 mW of Nd:YAG and Ti:Sa pump powers, respectively. This result can easily be pushed into the microwatt range by increasing pump powers and reducing scattering losses originating from processing; such power levels are interesting for mid-infrared spectroscopic applications. We note also that the generated wavelength (5.3 μm) is in the absorption range of $LiNbO_3$, where few nonlinear optical materials exist. Fourier-transform infrared spectroscopic measurements show that absorption losses in Alox start for wavelengths >7.5 μm, opening a very large spectral range for tunable DFG. The efficiency of this frequency converter is limited by the mid-infrared losses which are essentially due to scattering on the ridge inhomogeneities introduced during the technological process. Improving the technological process to reduce these losses will be very important for the success of this composite material in frequency conversion devices. The tunability of the mid-infrared wavelength was demonstrated by varying the temperature. We have measured a linear dependence of the signal wavelength from 5.2 to 5.6 μm with a temperature scan from 0 to 150 °C (Fig. 3 inset). No degradation of the sample was observed during temperature cycles.

The birefringence of the composite structure is sufficient not only to phase match DFG in the mid-infrared, but also for second-harmonic generation around 1.55 μm. We give these two examples because of their interest for applications: continuously tunable mid-infrared compact sources are desirable for pollutant detection in the molecular fingerprint region or for process monitoring, and a 1.55-μm signal can be shifted by mixing it with a 0.75-μm pump. The latter function is required in wavelength division multiplexing systems. Other possible implications go beyond use of the simple passive nonlinear material: GaAs is also the favoured material for quantum-well lasers, and the possibility of integrating quantum wells in the core of the nonlinear waveguide is under study. In a first step, this would enable DFG with only one external source, the other frequency being given by the 'internal' quantum-well laser. In a second step, parametric fluorescence from this laser would make a completely monolithic micro-optical parametric oscillator—on a GaAs chip, tunable with temperature—a realistic possibility. □

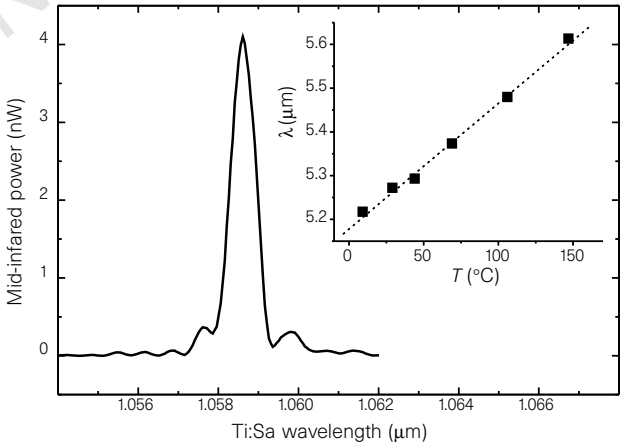

Figure 3 Mid-infrared DFG signal measured by an InSb detector, as a function of the wavelength of the Ti:Sa laser. The pump powers were 0.2 mW and 1.6 mW for the YAG and Ti:Sa lasers, respectively. This function has the well known shape of a phase matching resonance: it is a $((\sin x)/x)^2$ function, characteristic of momentum conservation in a fixed interaction length[3]. Inset, signal wavelength tunability with temperature.

Received 21 August; accepted 4 November 1997.

1. Armstrong, J. A., Bloembergen, N., Ducuing, J. & Pershan, P. S. Interactions between light waves in a non linear dielectric. *Phys. Rev.* **127,** 1918–1939 (1962).
2. Fejer, M. M. Nonlinear optical frequency conversion. *Phys. Today* **47(5),** 25–32 (1994).
3. Fejer, M. M., Magel, G. A., Jundt, D. H. & Byer, R. L. Quasi-phase-matched second harmonic generation: Tuning and tolerances. *IEEE J. Quant. Electron.* **28,** 2631–2654 (1992).
4. Myers, L. E. *et al.* Quasi-phase-matched 1.064-μm-pumped optical parametric oscillator in bulk periodically poled $LiNbO_3$. *Opt. Lett.* **20,** 52–54 (1995).
5. Thomson, D. E., McMullen, J. D. & Anderson, D. B. Second-harmonic generation in GaAs stack of plates using high power CO_2 laser radiation. *Appl. Phys. Lett.* **29,** 113–115 (1976).
6. Yoo, S. J. B. *et al.* Wavelength conversion by difference frequency generation in AlGaAs waveguides with periodic domain inversion achieved by wafer bonding. *Appl. Phys. Lett.* **68,** 2609–2611 (1996).
7. Van der Ziel, J. P. Phase-matched harmonic generation in a laminar structure with wave propagation in the plane of the layers. *Appl. Phys. Lett.* **26,** 60–62 (1975).
8. Rosencher, E. *et al.* Quantum engineering of optical non linearities. *Science* **271,** 168–173 (1996).
9. Born, E. & Wolf, E. *Principles of Optics* (Pergamon, Oxford, 1980).
10. Yeh, P. *Optical Waves in Layered Media* (Wiley, New York, 1988).
11. Joannopoulos, J. D., Villeneuve, P. R. & Fan, S. Photonic crystals: putting a new twist on light. *Nature* **386,** 143–149 (1997).

12. Dallesasse, J. M., Holonyak, J. N., Sugg, A. R., Richard, T. A. & El-Zein, N. Hydrolysation oxidation of AlGaAs-AlAs-GaAs quantum well heterostructures and superlattices. *Appl. Phys. Lett.* **57,** 2844–2846 (1990).
13. Huffaker, D. L., Deppe, D. G. & Kumar, K. Native-oxide defined ring contact for low-threshold vertical-cavity lasers. *Appl. Phys. Lett.* **65,** 97–99 (1994).
14. MacDougal, M. H., Zao, H., Dapkus, P. D., Ziari, M. & Steier, W. H. Wide-bandwidth distributed bragg reflectors using oxide/GaAs multilayers. *Electron. Lett.* **30,** 1147–1149 (1994).
15. Fiore, A. *et al.* $\Delta n = 0.22$ birefringence measurement by surface emitting second harmonic generation in selectively oxidized GaAs/AlAs optical waveguides. *Appl. Phys. Lett.* **71,** 2587–2589 (1997).

Acknowledgements. This work was partially supported by the European Community under the IT "OFCORSE" Programme.

Correspondence and requests for materials should be addressed to V.B. (e-mail: berger@thomson-lcr.fr).

Broken symmetry and pseudogaps in ropes of carbon nanotubes

Paul Delaney*, Hyoung Joon Choi*†, Jisoon Ihm*†, Steven G. Louie* & Marvin L. Cohen*

** Department of Physics, University of California at Berkeley, and Materials Sciences Division, Lawrence Berkeley National Laboratory, Berkeley, California 94720, USA*
† Department of Physics and Center for Theoretical Physics, Seoul National University, Seoul 151-742, Korea

Since the discovery of carbon nanotubes[1], it has been speculated that these materials should behave like nanoscale wires with unusual electronic properties and exceptional strength. Recently, 'ropes' of close-packed single-wall nanotubes have been synthesized in high yield[2]. The tubes in these ropes are mainly of the (10,10) type[3], which is predicted to be metallic[4–6]. Experiments on individual nanotubes and ropes[7,8] indicate that these systems indeed have transport properties that qualify them to be viewed as nanoscale quantum wires at low temperature. It has been expected that the close-packing of individual nanotubes into ropes does not change their electronic properties significantly. Here, however, we present first-principles calculations which show that a broken symmetry of the (10,10) tube caused by interactions between tubes in a rope induces a pseudogap of about 0.1 eV at the Fermi level. This pseudogap strongly modifies many of the fundamental electronic properties: we predict a semimetal-like temperature dependence of the electrical conductivity and a finite gap in the infrared absorption spectrum. The existence of both electron and hole charge carriers will lead to qualitatively different thermopower and Hall-effect behaviours from those expected for a normal metal.

Carbon nanotubes are tubular structures which are typically a few nanometres in diameter and many micrometres in length. These quasi-one-dimensional systems are predicted[4–6] to have an electronic structure dictated by their geometric structure. In particular, an isolated armchair-type nanotube (one whose roll-up indices are (n, n)) has two linear bands which cross at the Fermi level. These two linear bands give rise to a constant density of states near the Fermi level and to metallic behaviour in conduction and other physical properties. One of the bands has π-bonding and the other has π-antibonding character. An isolated (n, n) nanotube has n mirror planes containing the tube axis. The π-bonding state is even (the wavefunction has no sign change) and the π-antibonding state is odd (sign change) under these symmetry operations. The band crossing is allowed and the armchair nanotube is metallic as shown schematically in Fig. 1a. It is precisely this symmetry of the isolated (n, n) tube that gives its desired metallic behaviour[9], and this property motivates many of the recent electrical measurements. Breaking of this symmetry, however, will completely alter this picture.

With the rope axis vertical, if one were to separate the tubes in a rope far enough to eliminate any interactions between the tubes, then the energy bands of the rope would have no dispersion in the horizontal plane, and the band structure along any vertical line in reciprocal space would be identical to that of a single isolated tube, with a band crossing as shown in Fig. 1a. However, the actual distances between tubes in the ropes are small enough that each nanotube can feel the potential due to all the other nanotubes. As a result of this perturbation, the Hamiltonian at any point k where the two bands used to cross becomes

$$H_k = \begin{pmatrix} \epsilon_0 + \delta_{11} & \delta_{12} \\ \delta_{21} & \epsilon_0 + \delta_{22} \end{pmatrix} \quad (1)$$

where ϵ_0 is the unperturbed energy. The diagonal matrix elements δ_{11} and δ_{22} merely act to shift the energy and location in k-space of the band crossing. It is the off-diagonal elements that cause quantum-mechanical level repulsion and therefore open a gap as shown schematically in Fig. 1b. If the vertical line through k has high

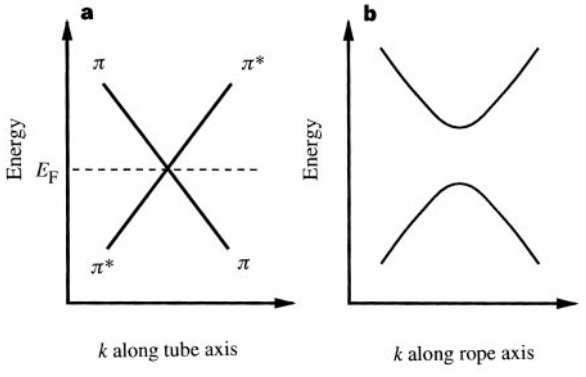

Figure 1 Band crossing and band repulsion. **a**, Schematic diagram of the crossing of two linear bands for an isolated (n,n) carbon nanotube. One band has π-bonding character and the other has π-antibonding (π^*) character. E_F is the Fermi energy and k is the wavevector. **b**, Repulsion of bands due to breaking of mirror symmetry.

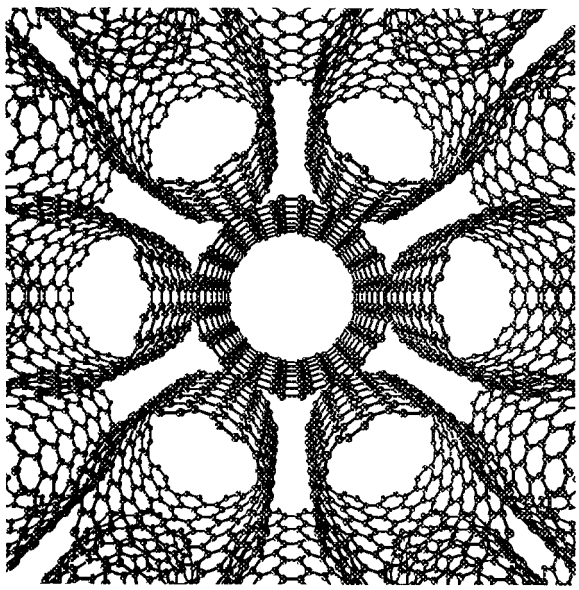

Figure 2 Perspective view of a rope of (10,10) carbon nanotubes. Along the horizontal axis one can see the alignment of the chains of hexagons between neighbouring nanotubes.